Impact of the altitudinal Joule heating distribution on the thermosphere

Yue Deng,[1] Timothy J. Fuller-Rowell,[2,3] Rashid A. Akmaev,[3] and Aaron J. Ridley[4]

Received 18 August 2010; revised 13 March 2011; accepted 6 April 2011; published 18 May 2011.

[1] The thermospheric response at satellite altitudes along low Earth orbit is subject to the energy deposition locally, i.e., at high altitudes, and the vertical wave propagation from the energy injection at lower altitudes. In this study, a general circulation model has been run to investigate the source of nonhydrostatic effects and the sensitivity of the vertical wind and neutral density at satellite orbits to the energy deposited at low and high altitudes. Through comparing the simulations with and without the Joule heating enhancement above 150 km altitude, the impact of the heating at low and high altitudes on the high-altitude thermosphere has been separated. The numerical simulations show that most of the nonhydrostatic effects at high altitudes (300 km) arise from sources below 150 km and propagate vertically through the acoustic wave. The heating above 150 km is responsible for a large increase of the average vertical velocity (40 m/s) and neutral density (50%) at 300 km and higher altitudes.

Citation: Deng, Y., T. J. Fuller-Rowell, R. A. Akmaev, and A. J. Ridley (2011), Impact of the altitudinal Joule heating distribution on the thermosphere, *J. Geophys. Res.*, *116*, A05313, doi:10.1029/2010JA016019.

1. Introduction

[2] The knowledge of the 3-dimensional (3-D) electrodynamics is very limited at present but highly desirable to the thermosphere response to the heating. Due to the observational constraints, the studies of high-latitude electrodynamics have been devised either in one dimension or two dimensions, e.g., the altitude-integrated conductivities and Joule heating [*Amm et al.*, 2008]. The existing instruments with 3-D capability include the networks of GPS for the 3-D ionospheric electron density [*Mitchell and Spencer*, 2003] and all-sky Fabry-Perot interferometers for the neutral winds and temperature at different altitudes [*Conde and Smith*, 1998]. The simultaneous observations of all the 3-D electrodynamic and plasma parameters including Joule heating are however not available, which is actually crucial to fully understand the coupling between magnetosphere and ionosphere. It is significant to explain the thermospheric upwelling at locations where the height-integrated Joule heating cannot properly deal with and the information about height distribution of the energy dissipation is needed [*Richmond*, 2010]. The missions, such as the Advanced Modular Incoherent Scatter Radar (AMISR) project, will enable us to take into account variations in all three dimensions simultaneously [*Amm et al.*, 2008]. Therefore, it is timely to investigate the influence of the altitudinal Joule heating distribution on the thermosphere using a theoretical model.

[3] Accurate description of both the total amount electromagnetic energy from the magnetosphere and the spatial distribution of this energy is significant to understand how the upper atmosphere responds. Many studies have been conducted for the polar distributions of the 2 dimensional altitude-integrated Joule heating [*Lu et al.*, 1995; *Thayer et al.*, 1995; *Matsuo et al.*, 2005; *McHarg et al.*, 2005; *Richmond*, 2010]. However, very little previous work has been devoted to the altitudinal distribution of Joule heating. The simulation results by *Deng et al.* [2008a] showed that the same total energy with different altitudinal distribution causes significant difference in the thermosphere. In the observations, attention has been paid to the altitude-resolved Joule heating at E region altitudes [*Thayer*, 1998], since the deposited energy in the form of Joule heating peaks at E region altitudes. The direct influence of Joule heating on temperature (Joule heating per unit mass) is however largest in the F region due to the exponential decrease of neutral density with altitude. Previous studies [*Hays et al.*, 1973; *Heelis and Coley*, 1988] have also pointed out the significance of heating in the upper thermosphere for the large vertical motion and density disturbance.

[4] After a sudden enhancement of the ion convection, Joule heating increases at all altitudes due to the enhancement of the difference between the ion drift and neutral wind velocity. The thermospheric response at high altitudes is thus affected by energy changes at both E region and F region altitudes through the thermal expansion and atmospheric upwelling [*Prölss*, 1981; *Lühr et al.*, 2004]. It is, however, not clear whether the vertical wind and the

[1]Department of Physics, University of Texas at Arlington, Arlington, Texas, USA.
[2]CIRES, University of Colorado at Boulder, Boulder, Colorado, USA.
[3]Space Weather Prediction Center, NOAA, Boulder, Colorado, USA.
[4]Center for Space Environment Modeling, University of Michigan, Ann Arbor, Michigan, USA.

0148-0227/11/2010JA016019

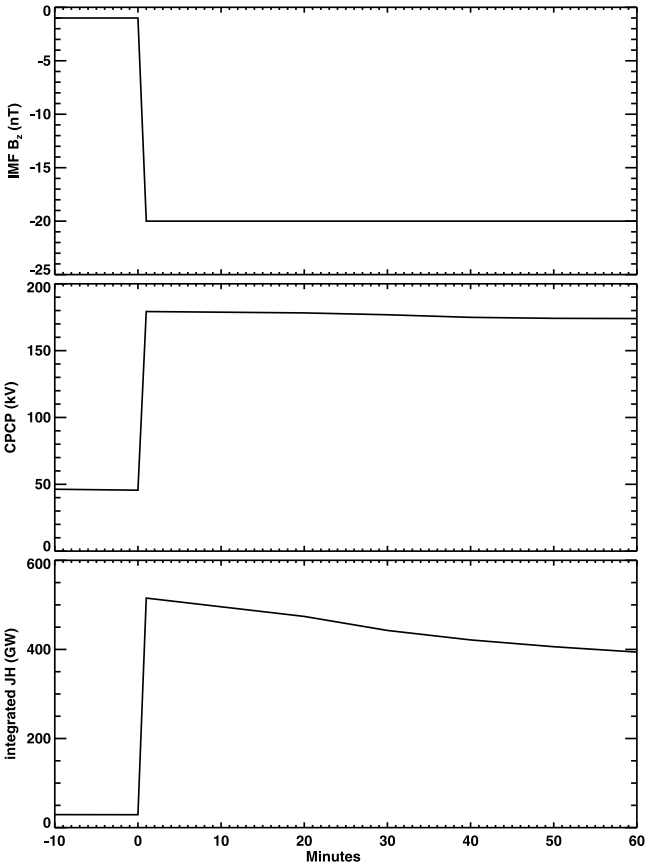

Figure 1. Temporal variation of IMF (top) B_z, (middle) CPCP, and (bottom) hemisphere-integrated Joule heating in the Southern Hemisphere. Zero in the x axis represents 0600 UT.

neutral density variation in the low Earth satellite orbits is primarily caused by the energy deposited at low altitudes or at high altitudes. In this study, a general circulation model (GCM) has been employed to investigate the source of nonhydrostatic effects [*Deng et al.*, 2008b] and sensitivity of the vertical wind and neutral density at satellite orbits to the energy deposited at both low and high altitudes in the aurora region after a significant heating increase. The measurements of 3-D Joule heating are not available at present and our study may serve as a theoretical reference for future observations.

2. Global Ionosphere Thermosphere Model

[5] Global Ionosphere Thermosphere Model (GITM) is a three-dimensional spherical code that models the Earth's thermosphere and ionosphere system using a stretched grid in latitude and altitude [*Ridley et al.*, 2006]. It explicitly solves for the neutral and ion densities, velocities and temperatures self-consistently. The equations are based on the Navier-Stokes equations and are listed in the appendix of *Deng and Ridley* [2006]. The first-type boundary conditions are used for the lower boundary and specified by the MSIS and IRI empirical models. The second-type boundary conditions are used for the upper boundary and the derivatives are the same as those on the last inside cells.

[6] The simulations are started from MSIS and IRI, with static neutrals. The IGRF magnetic field with APEX coordinate system [*Richmond*, 1995] has been used. GITM can be coupled to a large number of models of the high-latitude ionospheric electrodynamics. In this study, it uses the electrodynamic potential patterns from *Weimer* [1996] and the particle precipitation patterns from *Fuller-Rowell and Evans* [1987] empirical models for the idealized conditions. The inputs into GITM include F10.7, Hemispheric Power (HP), interplanetary magnetic field (IMF) and solar wind conditions. The F10.7 index is used to calculate the solar ionization and absorption of the atmosphere to the solar irradiation. The HP index is utilized to drive the [*Fuller-Rowell and Evans*, 1987] empirical model, which specifies the particle precipitation patterns for GITM. The IMF and solar wind conditions are for the input of [*Weimer*, 1996] empirical model, which specifies the electrodynamic potential patterns for GITM.

[7] The most significant differences between GITM and other models is that GITM is a nonhydrostatic model with flexible resolution. In GITM, the hydrostatic approximation is relaxed and the vertical momentum is solved directly, which allows the acoustic wave to be assimilated in a GCM. A stretched grid in latitude and altitude has been used and the number of grid points in each direction can be specified, so the resolution is extremely flexible in GITM. The spatial resolution for this study is 5° longitude by 5° latitude by one third scale height, which is close to 250 km longitude by 500 km latitude by 5 km altitude in the aurora zone at 120 km altitude. There are some limitations to the GITM code. For example, GITM takes an approximately 2 seconds time step, while the typical time step for hydrostatic GCMs is close to 2–5 minutes. This small time step is the result of using explicit solver and resolving the vertical momentum equation and the sound speed in the region with tight resolution.

3. Results: Joule Heating at Low Altitudes Versus High Altitudes

[8] GITM has been run for 30 h of simulation time (from 0000 UT 28 October to 0600 UT 29 October), reaching a quasi steady state with relatively quiet geomagnetic conditions (IMF $B_z = -1.0$ nT, HP = 3.0 GW and F10.7 = 100.0×10^{-22} W/m^2/Hz). As shown in Figure 1, the IMF B_z is then changed to −20.0 nT at 0600 UT with the other input parameters remaining the same. The cross polar cap potential (CPCP) correspondingly increases from 45.0 kv to 158.0 kv in the Southern Hemisphere. Due to the correlation between IMF B_z and the energy input from the magnetosphere to the ionosphere, the hemispheric integrated Joule heating increases abruptly by a factor of 19.

[9] Figure 2 shows the distribution of altitude-integrated Joule heating in the Southern Hemisphere for both quiet time and active time, which is overplotted with the ion convection pattern at 300 km altitude. When the IMF B_z changes from −1 nT to −20 nT, the ion convection has enhanced and expanded to low latitudes. The altitude-integrated Joule heating increases by more than 10 times in the enhanced convection region, which results in a large

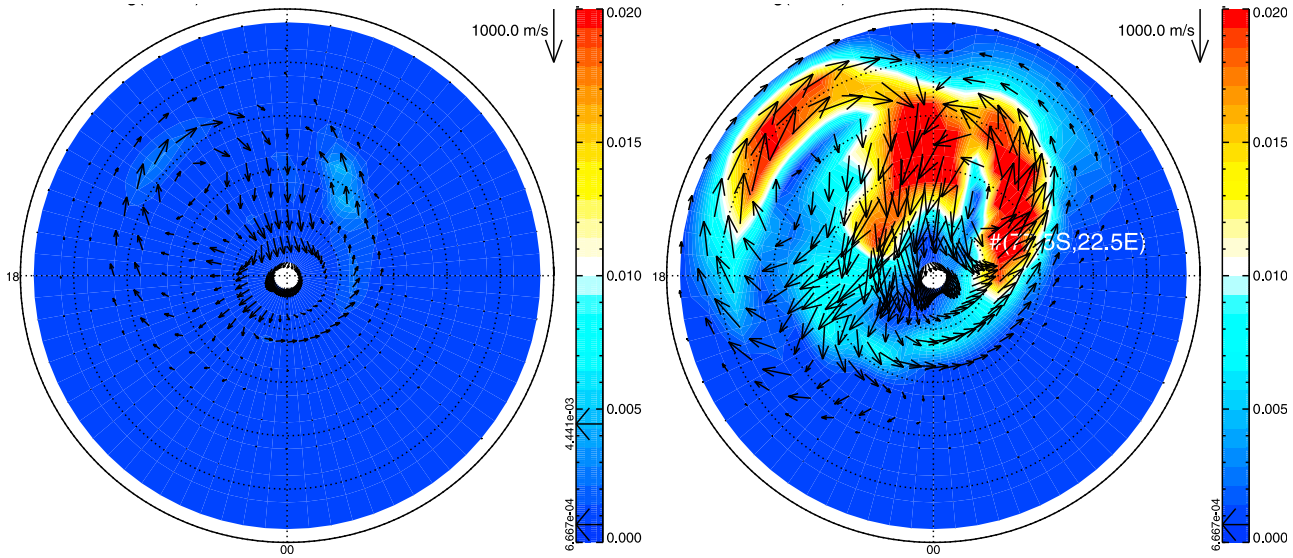

Figure 2. The color contour shows the altitudinal integrated Joule (W/m^2) heating in the Southern Hemisphere at (left) quiet time and (right) active time. The vectors represent the corresponding ion convection. The specific position (77.5°S, 22.5°E), which has been examined in Figures 3 and 4, is marked with a # sign. The outside ring is −40°.

area with more than 0.02 W/m^2 of Joule heating. One particular location (77.5° S, 22.5° E), which is marked in Figure 2 and is close to the Joule heating peak, has then been chosen for detailed study.

[10] In order to separate the impact of energy input at low and high altitudes, we have compared two idealized runs with (case 1) or without (case 2) Joule heating enhancement above the cutting altitude at 150 km. In case 1, Joule heating is calculated with the enhanced ion convection at all altitudes. In case 2, Joule heating below 150 km has been calculated in the same way as case 1, while Joule heating above 150 km is specified with the quiet time values. Case 2 represents the situation when the heating enhances at low altitudes alone. The difference between case 1 and case 2 is technically similar to the case when the heating enhances at high altitudes alone. We set the cutting altitude at 150 km because it roughly separates the E region and the F region. Figures 3 and 4 show the temporal variation of the altitudinal distribution of Joule heating, buoyancy acceleration, vertical velocity and neutral density at (77.5° S, 22.5° E) in both cases. The line plots represent the temporal variations at 300 km altitude. It is not intended to focus on the Southern Hemisphere since this is just a theoretical study. The simulation time happens to be 29 October when the subsolar point is in the Southern Hemisphere. Due to the higher conductance, Joule heating in the Southern Hemisphere is therefore larger than that in the Northern Hemisphere and the effect we study is expected to be larger. If the analysis focuses on the Northern Hemisphere, similar conclusions should be reached except some quantitative change in the results due to the smaller Joule heating enhancement.

[11] Figure 3a shows that the maximum Joule heating in case 1 is at 120 km altitude and increases from 7.9×10^{-8} W/m^3 to 1.3×10^{-6} W/m^3 when the ion convection increases. The Joule heating at 300 km is almost 2 orders of magnitude smaller and also increases with the ion convection. Our calculation shows that approximately 25% of the total Joule heating is deposited above 150 km and 75% is deposited below that level. For example, at 0610UT, the total altitude-integrated Joule heating is close to 0.03 W/m^2 and the integrated Joule heating from the lower boundary to 150 km is ~0.022 W/m^2. The total Joule heating in case 2 is ~ 25% smaller than that in case 1 due to the method difference. The buoyancy acceleration ($-\frac{1}{\rho}\frac{\partial P}{\partial r} + g_r$), the difference between the pressure gradient force per unit mass and gravity acceleration, is equal to zero under the hydrostatic assumption, which approximately holds before 0600 UT, as shown in Figure 3b. But it increases at all altitudes after the energy enhancement for both cases, and the value is larger than 2.0 m/s^2 near the upper boundary. The gravitational acceleration at 400 km altitude is ~8.7 m/s^2, and the pressure gradient force per unit mass is thus ~10.7 m/s^2, which is 23% larger than the gravity acceleration. Both cases show that after the sudden enhancement of Joule heating a strong disturbance of buoyancy acceleration propagates vertically with exponentially increasing magnitude resulting in the maximum disturbance at high altitudes. The significant difference between the two cases is the disturbance before the positive maximum. Due to the heating above 150 km, there is a clear positive disturbance between 0600 and 0603 UT at 300 km in case 1, but not in case 2. The difference at 0603 UT is more than 1.0 m/s^2, which results in large differences in the vertical velocity.

[12] The vertical velocity is related to a temporal integration of the vertical acceleration. Figure 4a shows that

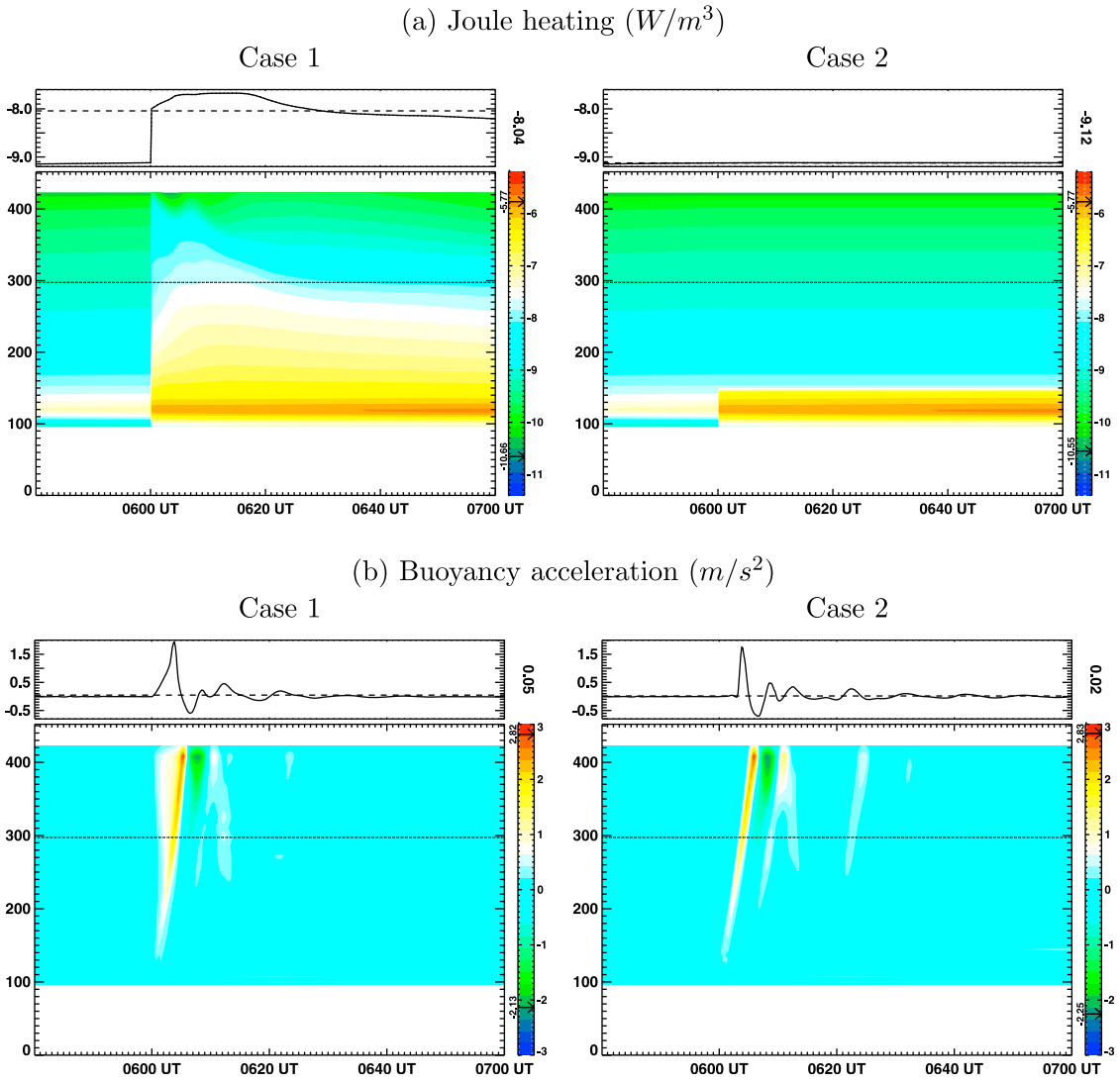

Figure 3. (a) The temporal variation of the altitudinal profiles of Joule heating per unit volume (W/m^3) at (77.5°S, 22.5°E) for (left) case 1 and (right) case 2. The location has been marked in Figure 2. The numbers and arrows attached to the color bars indicate the minimum and maximum values in the color contour. The line plots on top show the variations at 300 km altitude and the numbers on the right-hand side represent the average value of the corresponding line plots. (b) Same as Figure 3a except for the buoyancy acceleration ($-\frac{1}{\rho}\frac{\partial P}{\partial r} + g_r$) (m/s^2). The Joule heating (Figure 3a) is plotted on a logarithmic scale, and the buoyancy acceleration (Figure 3b) is plotted on a linear scale.

the maximum vertical wind at 300 km in case 1 is above 150.0 m/s and almost 3 times larger than that in case 2. Both cases have similar temporal variations at 300 km, and the biggest difference between them is the 1 h average vertical velocity, which is 43.6 m/s in case 1 and 3.5 m/s in case 2. This difference indicates that the heating above 150 km (25% of the total energy) has a stronger influence on the steady expansion of the atmosphere at high altitudes than the heating below 150 km (75% of the total energy). The heating at high altitudes sets up a large vertical wind, which is overlapped by a disturbance propagating from the lower altitudes. While the acoustic wave propagating vertically from lower altitudes can cause a large buoyancy acceleration at 300 km, it mainly imposes some temporal variation on the vertical velocity. Figure 4b shows that case 1 also has a much larger density increase than case 2 and the average difference between them at 300 km altitude is ~ 50% of the background value. Since the thermosphere/ionosphere is a nonlinear system, the variation of neutral density causes additional changes in the system, such as the absorption of solar irradiation, neutral dynamics and ionospheric density, which in turn feed back to the neutral density. In this paper, the time scale we are concerned with is the first hour after the energy enhancement, and all secondary effects on the neutral density are not discussed. Figure 3b and Figure 4a show a reflection at the upper boundary, which happens in most simulations with general boundary conditions when no addition wave damping layer has been added on top. It is numerical and not physically meaningful. Since the neutral density exponentially decreases with altitude and the wave is damped quickly when propagating downward, this reflection is smaller than the disturbance propagating from

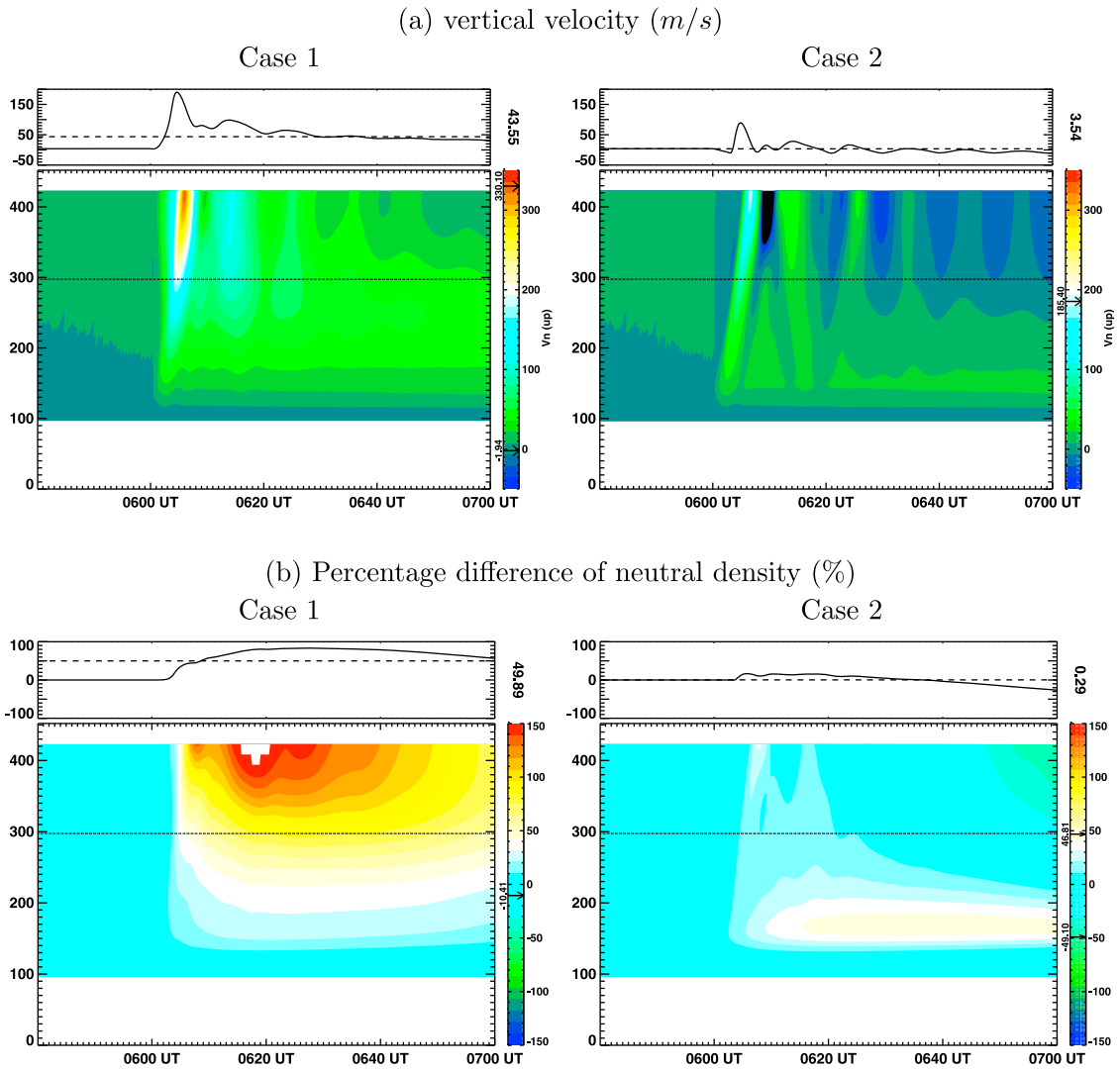

Figure 4. The same as Figure 3 except for the (a) vertical velocity (m/s) and (b) the percentage difference of neutral density compared with the value in the background case, respectively.

lower altitudes and will not change the main conclusion of our study.

[13] Figures 3 and 4 only represent the results at one specific location (77.5° S, 22.5° E). In order to examine the neutral density variation in the whole high-latitude region, the polar distributions at 0700 UT for both cases have been shown in Figure 5. Figure 5a depicts the neutral density and neutral wind vectors at 130 km altitude in the Southern Hemisphere. Clearly, there are a density maximum peak at −55° latitude and 14 LT and a minimum peak at −75° latitude and 11 LT in case 1. The density maximum and minimum peaks are overlapped with the vortex centers very well in both cases. This two-peak structure in the neutral density has been reported in both observations [*Kwak et al.*, 2009] and simulations [*Crowley et al.*, 2006], and explained as the results of the neutral dynamics. When the ion convection is enhanced, the increase of cyclonic (anticyclonic) wind vortex on the dawnside (duskside) tends to have a low (high) pressure and density at its center.

[14] At 300 km altitude, the two-peak structure is persistent and two cases have similar distributions, except that the magnitude of the neutral density in case 2 is consistently smaller than that in case 1. The percentage difference of the neutral density compared with the background run, in which the IMF B_z is kept as constant (B_z = −1.0 nT), has been calculated. As shown in Figure 5c, the percentage difference of neutral density in the whole polar region is positive in case 1. The distribution mimics the structure shown in Figure 5a, with a minimum peak at 11 LT and a maximum peak at 13 LT. Case 2 has a very similar distribution as case 1 except that the magnitude is on average 50% smaller. This discrepancy is consistent with the neutral density difference at (77.5° S, 22.5° E). As shown in Figure 4b, the average neutral density percentage enhancements in case 1 and case 2 are 49.89% and 0.29%, respectively. Therefore the difference between these two cases is also ~ 50%. In case 2, in order to separate the effect of Joule heating from other mechanisms, Joule heating above 150 km has been specified as the background values and all other parameters change with IMF variation. This method creates inconsistency between the Joule heating and convection, and the hori-

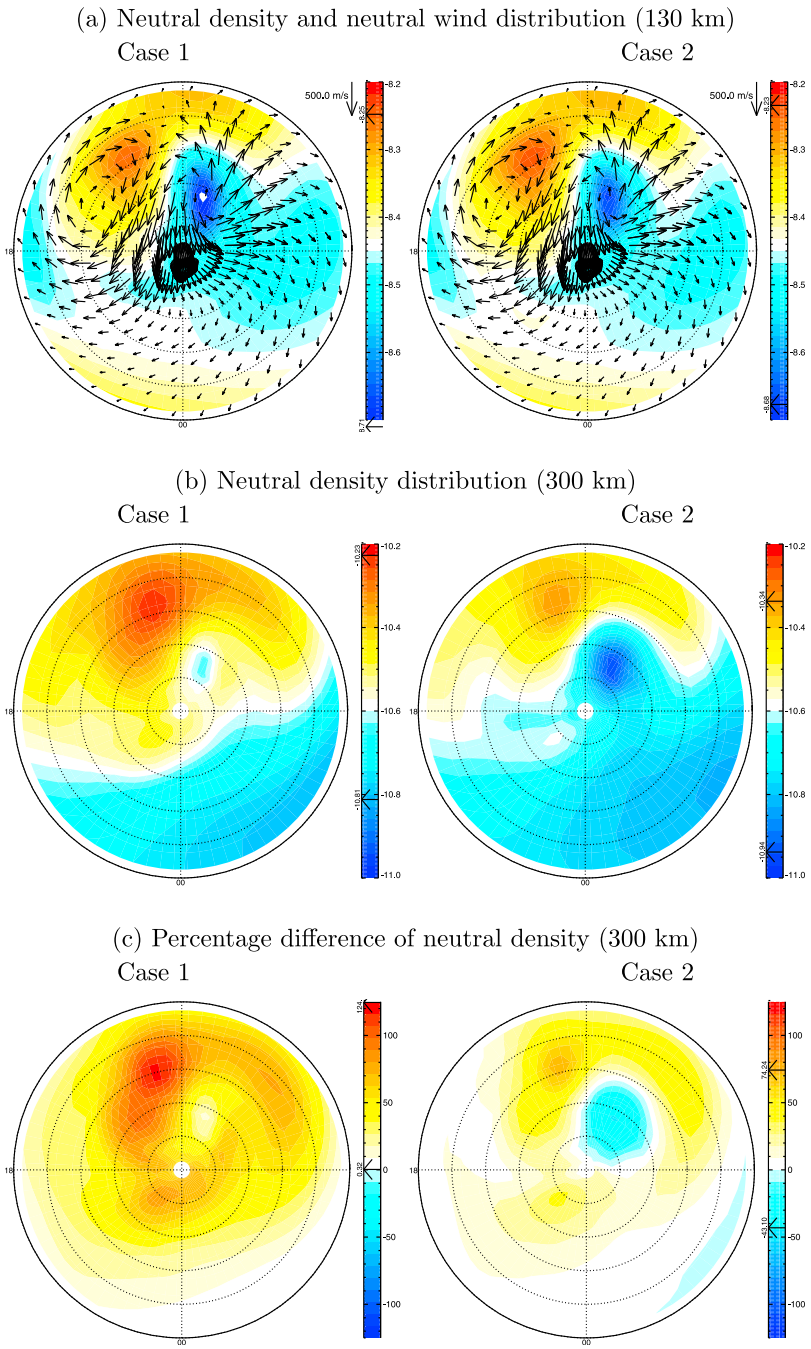

Figure 5. (a) Neutral density distribution at 130 km altitude at 0700 UT in the Southern Hemisphere. The neutral wind velocity vectors are plotted out on top of the neutral density and the outside ring is −40°. (b) Neutral density distribution at 300 km altitude at 0700 UT in the Southern Hemisphere. (c) The same as Figure 5b except for the percentage difference of neutral density at 300 km compared with the background case.

zontal winds above 150 km in case 2 are not very physically meaningful.

[15] After about 20 minutes of forcing, Figure 4 shows a gradual downward trend in density in both case 1 and 2. Figure 5 indicates that part of this trend is likely to be dependent on the particular location chosen, and whether or not it is experiencing the cooling effect from the divergent vortex on the dawnside. This modulation of density by the dynamics of the vortices is comparable with the large differences in density between case 1 and 2 at the specific location (77.5° S, 22.5° E).

4. Summary

[16] After a sudden enhancement of the ion convection, the Joule heating increases at all altitudes due to the increase

of the difference between the ion drift and neutral wind. The largest enhancement of energy in the form of Joule heating happens at E region altitudes, the influence on temperature (Joule heating per unit mass) is however largest in the F region since the neutral density decreases with altitude exponentially. The thermospheric response at CHAMP and GRACE satellite orbits (400–500 km) is thus subject to the energy variation locally, i.e., at high altitudes, and the vertical wave propagation from the energy injection at lower altitudes. In this study, a GCM has been employed to investigate the source of nonhydrostatic processes and the sensitivity of the vertical wind and neutral density at high altitudes to the energy deposited at low and high altitudes.

[17] Through comparing the simulations with and without the Joule heating enhancement above 150 km altitude, the impact of the heating at low and high altitudes to the high-altitude thermosphere has been separated. The numerical simulations show that the atmosphere at all altitudes is out of hydrostatic equilibrium after the sudden energy enhancement. But most of the nonhydrostatic effects at high altitudes (300 km) arise from sources below 150 km in the form of an acoustic wave propagating vertically. The heating at high altitudes sets up a large vertical wind, which is overlapped by a disturbance propagating from the low altitudes. While the disturbance propagating vertically from low altitudes can cause a large buoyancy acceleration at 300 km, it mainly brings some temporal variation to the vertical velocity. The heating above 150 km is the primary source for a large increase of the average vertical velocity (40 m/s) and neutral density (50%) at 300 km and higher altitudes. Although the case studied represents an extreme situation, it shows that the energy deposited at high altitudes has a stronger influence on the neutral density variation at F region altitudes than the energy deposited at low altitudes.

[18] The idealized experiments we have done help us to understand the thermospheric response to the altitudinal distribution of heating. The same amount of energy deposited at different altitudes will cause very different thermospheric results. Therefore, the altitude-resolved energy distribution, especially in the F region, is very desirable for precise description of the thermospheric response. Because Joule heating is the dominant energy transport process from the magnetosphere to the thermosphere/ionosphere, we investigated only its effects in this theoretical study. The general results however are not limited to this particular energy input method and should also apply to the enhancement of particle heating and other energy sources.

[19] This work is an idealized study of the impact of the altitudinal distribution of Joule heating on the thermosphere. For example, the Joule heating below and above 150 km altitude are totally decoupled in case 2. In reality, the Joule heating is distributed in altitude roughly proportional to the Pedersen conductivity and correlated well between different altitudes as shown in Figure 3a. Meanwhile, this study investigates only the first hour after the heating increase because during that period the response of the thermosphere primarily presents the direct effect of the heating enhancement. Other mechanisms included in the model, such as molecular heat conduction, can transfer heat vertically and play an important role in the altitudinal energy distribution at longer time scales.

[20] **Acknowledgments.** This research was supported by the University Colorado at Boulder CIRES Visiting Fellows Program. It was also supported by NSF through grants ATM0955629 and ATM0823689.

[21] Robert Lysak thanks the reviewers for their assistance in evaluating this paper.

References

Amm, O., et al. (2008), Toward understanding the electrodynamics of the 3-dimensional high-latitude ionosphere: Present and future, *Ann. Geophys.*, *26*, 3913–3932.

Conde, M., and R. W. Smith (1998), Spatial structure in the thermospheric horizontal wind above Poker Flat, Alaska, during solar minimum, *J. Geophys. Res.*, *103*, 9449–9472.

Crowley, G., T. J. Immel, C. L. Hackert, J. Craven, and R. G. Roble (2006), Effect of IMF B_Y on thermospheric composition at high and middle latitudes: 1. Numerical experiments, *J. Geophys. Res.*, *111*, A10311, doi:10.1029/2005JA011371.

Deng, Y., and A. J. Ridley (2006), Dependence of neutral winds on convection E-field, solar EUV, and auroral particle precipitation at high latitudes, *J. Geophys. Res.*, *111*, A09306, doi:10.1029/2005JA011368.

Deng, Y., A. Maute, A. D. Richmond, and R. G. Roble (2008a), Analysis of thermospheric response to magnetospheric inputs, *J. Geophys. Res.*, *113*, A04301, doi:10.1029/2007JA012840.

Deng, Y., A. D. Richmond, A. J. Ridley, and H.-L. Liu (2008b), Assessment of the non-hydrostatic effect on the upper atmosphere using a general circulation model (GCM), *Geophys. Res. Lett.*, *35*, L01104, doi:10.1029/2007GL032182.

Fuller-Rowell, T. J., and D. Evans (1987), Height-integrated Pedersen and Hall conductivity patterns inferred from TIROS–NOAA satellite data, *J. Geophys. Res.*, *92*, 7606–7618.

Hays, P. B., R. A. Jones, and M. H. Rees (1973), Auroral heating and the composition of the neutral atmosphere, *Planet. Space Sci.*, *21*, 559–573.

Heelis, R. A., and W. R. Coley (1988), Global and local Joule heating effects seen by DE 2, *J. Geophys. Res.*, *93*, 7551–7557.

Kwak, Y., A. D. Richmond, Y. Deng, J. M. Forbes, and K. Kim (2009), Dependence of the high-latitude thermospheric densities on the interplanetary magnetic field, *J. Geophys. Res.*, *114*, A05304, doi:10.1029/2008JA013882.

Lu, G., et al. (1995), Characteristics of ionospheric convection and field-aligned current in the dayside cusp region, *J. Geophys. Res.*, *100*, 11,845–11,861.

Lühr, H., M. Rother, W. Köhler, P. Ritter, and L. Grunwaldt (2004), Thermospheric up-welling in the cusp region: Evidence from CHAMP observations, *Geophys. Res. Lett.*, *31*, L06805, doi:10.1029/2003GL019314.

Matsuo, T., A. D. Richmond, and G. Lu (2005), Optimal interpolation analysis of high-latitude ionospheric electrodynamics using empirical orthogonal functions: Estimation of dominant modes of variability and temporal scales of large-scale electric fields, *J. Geophys. Res.*, *110*, A06301, doi:10.1029/2004JA010531.

McHarg, M., F. Chun, D. Knipp, G. Lu, B. Emery, and A. Ridley (2005), High-latitude Joule heating response to IMF inputs, *J. Geophys. Res.*, *110*, A08309, doi:10.1029/2004JA010949.

Mitchell, C. N., and P. S. J. Spencer (2003), A three-dimensional time-dependent algorithm for ionospheric imaging using GPS, *Ann. Geophys.*, *46*, 687–696.

Prölss, G. W. (1981), Latitudinal structure and extension of the polar atmospheric disturbance, *J. Geophys. Res.*, *86*, 2385–2396.

Richmond, A. D. (1995), Ionospheric electrodynamics using magnetic apex coordinates, *J. Geomagn. Geoelectr.*, *47*, 191–212.

Richmond, A. D. (2010), On the ionospheric application of Poynting's theorem, *J. Geophys. Res.*, *115*, A10311, doi:10.1029/2010JA015768.

Ridley, A. J., Y. Deng, and G. Toth (2006), The global ionosphere-thermosphere model, *J. Atmos. Sol. Terr. Phys.*, *68*, 839–864.

Thayer, J. P. (1998), Height-resolved Joule heating rates in the high-latitude *E* region and the influence of neutral winds, *J. Geophys. Res.*, *103*, 471–487.

Thayer, J. P., J. F. Vickrey, R. A. Heelis, and J. B. Gary (1995), Interpretation and modeling of the high-latitude electromagnetic energy flux, *J. Geophys. Res.*, *100*, 19,715–19,728.

Weimer, D. R. (1996), A flexible, IMF dependent model of high-latitude electric potential having "Space Weather" applications, *Geophys. Res. Lett.*, *23*, 2549–2552.

R. A. Akmaev and T. J. Fuller-Rowell, Space Weather Prediction Center, NOAA, 325 Broadway, Boulder, CO 80305, USA. (rashid.akmaev@noaa.gov; tim.fuller-rowell@noaa.gov)

Y. Deng, Department of Physics, University of Texas at Arlington, 502 Yates St., Arlington, TX 76019, USA. (yuedeng@uta.edu)

A. J. Ridley, Center for Space Environment Modeling, University of Michigan, Ann Arbor, MI 48109, USA. (ridley@umich.edu)